



Electrocatalysis of oxygen reduction reaction on polyaniline-derived nitrogen-doped carbon nanoparticle surfaces in alkaline media

Nemanja Gavrilov^a, Igor A. Pašti^a, Miodrag Mitrić^b, Jadranka Travas-Sejdić^{c,d}, Gordana Čirić-Marjanović^a, Slavko V. Mentus^{a,e,*}

^a University of Belgrade, Faculty of Physical Chemistry, Studentski trg 12–16, 11158 Belgrade, Serbia

^b University of Belgrade, Vinča Institute of Nuclear Sciences, P.O. Box 522, 11001 Belgrade, Serbia

^c Polymer Electronics Research Centre, School of Chemical Sciences, University of Auckland, 23 Symonds Street, Auckland, New Zealand

^d MacDiarmid Institute for Advanced Materials and Nanotechnology, Victoria University of Wellington, P.O. Box 600, Wellington 6140, New Zealand

^e Serbian Academy of Sciences and Arts, Knez Mihailova 35, 11000 Belgrade, Serbia

HIGHLIGHTS

- Nitrogen-doped carbon nanomaterials were synthesized from polyaniline salts.
- Electrocatalytic activity toward ORR in alkaline solution was examined.
- Electrochemical data were correlated to the structural and textural data.
- Excellent electrocatalytic activity was found for carbonized PANI 5-sulfosalicylate.
- Electrocatalytic activity was correlated to electrical double layer capacity.

ARTICLE INFO

Article history:

Received 16 May 2012

Received in revised form

12 July 2012

Accepted 31 July 2012

Available online 9 August 2012

Keywords:

Carbonized polyaniline

Electrocatalyst

Nitrogen-containing carbon nanostructures

Oxygen reduction reaction

Surface functional groups

Textural properties

ABSTRACT

Nitrogen-doped carbon nanomaterials were synthesized by the carbonization of three different nanostructured polyaniline (PANI) salt precursors: PANI 3,5-dinitrosalicylate nanorods, PANI 5-sulfosalicylate nanorods/nanotubes, and PANI hydrogen sulfate nanorods/nanotubes/nanosheets. A comparative study of the electrocatalytic activity of these materials for oxygen reduction reaction (ORR) in alkaline solution was performed by using rotating disk electrode voltammetry. The electrochemical data were correlated to the structural and textural data obtained by Raman spectroscopy, X-ray diffractometry, X-ray photoelectron spectroscopy, elemental analysis and nitrogen sorption analysis. A fine interplay of textural characteristics, overall content of surface nitrogen and content of specific surface nitrogen functional groups were found to be responsible for a considerable variations in electrocatalytic properties toward ORR, involving variations in apparent number of electrons exchanged per O₂ molecule (from 2 to nearly 4) and variations in onset potential. The catalyst loading was found to influence remarkably the ORR kinetics. The excellent electrocatalytic activity was found for carbonized PANI 5-sulfosalicylate. Namely, it exhibited the most positive onset potential amounting to –0.05 V vs. SCE at a catalyst loading of 500 µg cm⁻². The interrelation between the electrocatalytic activity and the electrical double layer charging/discharging characteristics of the investigated N-doped nanocarbon materials was revealed.

© 2012 Elsevier B.V. All rights reserved.

1. Introduction

High efficiency and environmental friendliness of low-temperature fuel cells as a promising power source for various applications have stimulated extensive research in recent years

* Corresponding author. University of Belgrade, Faculty of Physical Chemistry, Studentski trg 12–16, 11158 Belgrade, Serbia. Tel./fax: +381 11 2187133.

E-mail address: slavko@ffh.bg.ac.rs (S.V. Mentus).

[1,2]. High cost and scarcity of platinum, used in both cathode and anode catalyst layer, and limited durability of electrode materials limit a commercial application of fuel cells. Therefore, research was recently focused on the reduction of the use of platinum, up to its full substitution by nonprecious catalysts. Among various electrocatalysts, either metal-doped or pure nitrogen-containing carbon nanostructures (NCNS), were investigated as a suitable alternative [3,4]. Numerous research groups reported recently a high electroactivity of N-containing carbon-based catalysts toward oxygen

reduction reaction (ORR) [4–11]. Some of the authors stressed that the presence of metals during the preparation of the catalysts plays an important role in the electrocatalytic activity [5,6]. Other studies suggested that pyridinic nitrogen acts as the major active site for ORR [7–9]. Nonetheless, the nature of the active sites for oxygen reduction in catalysts based on N-containing carbon materials remained still disputable [12–21]. Besides fuel cell application, the use of N-containing carbon materials as cathode materials in metal-air batteries presents nowadays an attractive field of research [22–24].

Commonly reported procedures for NCNS synthesis, such as post synthesis modification of carbon nanostructures with nitrogen-containing organic molecules [25–27] or laser ablation [28,29] and arc discharge [30,31] of graphite in the presence of a nitrogen source, usually require sophisticated equipment which is not suitable for large-scale production. On the other hand, NCNS can be easily prepared by a pyrolysis of N-containing organometallic macromolecules [6,9,32–36] or nitrogen-containing organic molecules [22,34,37–40]. Carbonization of nitrogen-containing aromatic polymer nanomaterials such as PANI nanostructures (which may simply be prepared under moderate and well controlled conditions by using both template-based and template-free methods [41]), was reported to be a proper way to prepare NCNS retaining the morphology of the nanostructured precursor [10,42–45]. It has recently been suggested [46] that the type of nanostructured PANI salt precursors used for preparation of NCNS determines special chemical, physical and textural properties of the obtained nanomaterials and, consequently, their performance in various applications, such as charge storage and electrocatalysis. It was also proposed that highly active catalysts could be obtained from structurally/morphologically optimized polymer precursors [46]. However, any systematic study in that sense did not appear in the literature until now.

The purpose of the present study was to compare the electrocatalytic activities of different carbonized PANI nanostructures toward ORR in alkaline media. Carbonized PANI hydrogen sulfate (C-PANI) nanorods/nanotubes/nanosheets [42,44], carbonized PANI 5-sulfosalicylate (C-PANI.SSA) nanorods/nanotubes [10], and carbonized PANI 3,5-dinitrosalicylate (C-PANI.DNSA) nanorods [45] were selected because they are expected to provide similar molecular structure and morphology, and, at the same time, crucial differences in textural properties, surface nitrogen and carbon concentration. The question of how diverse pore structures and nitrogen surface functional groups of similar N-containing carbon nanomaterials influence their different activity toward ORR is addressed for the first time in detail.

2. Experimental

2.1. Materials

Aniline (p.a., Centrohem, Serbia) was distilled under reduced pressure and stored under argon prior to use, in order to remove the impurities (e.g. aniline dimers, formed by aerial oxidation during prolonged storage of commercially available aniline) which may significantly influence the course of aniline oxidative polymerization [41].

Ammonium peroxydisulfate (APS), 5-sulfosalicylic acid (SSA) dihydrate and 3,5-dinitrosalicylic acid (DNSA) of analytical grade were used as received from Centrohem (Serbia).

N-containing nanostructured carbon materials, C-PANI, C-PANI.SSA and C-PANI.DNSA, were prepared via the gram-scale syntheses of PANI precursors and subsequent carbonization [10,42,45]. Nanostructured PANI precursors were synthesized by the template-free oxidative polymerization of aniline with ammonium

peroxydisulfate (APS) as an oxidant in three different media: 1. in water, without added acid (nanoPANI), 2. in the aqueous solution of SSA (nanoPANI-SSA), and 3. in the aqueous solution of DNSA (nanoPANI-DNSA). The nanoPANI precursor, containing hydrogen sulfate anions as prevalent counter-ions, was prepared according to the recently reported procedure [11,42]: the aqueous solutions of aniline (18.6 g, 500 ml) and oxidant APS (57.05 g, 500 ml) were mixed to start the oxidation, and the reaction mixture was stirred for 2 h. The precipitated nanoPANI was collected on a filter, rinsed with 5×10^{-3} M sulfuric acid and dried in vacuum. The nanoPANI.SSA precursor was prepared by the modified procedure [10] of Janošević et al. [47]: 12.26 g of aniline was dissolved in 1140 ml of aqueous solution containing 8.39 g SSA and the solution was heated to boiling, cooled to room temperature, then the aqueous solutions of monomer and oxidant APS (30.12 g, 600 ml) were mixed to start the oxidation, and the reaction mixture was stirred for 24 h. The precipitated nanoPANI.SSA was collected on a filter, rinsed with 5×10^{-3} M SSA and dried in vacuum. The modification enabled a rapid synthesis of larger quantities of the sample needed for its detailed characterization performed in this study. The modified procedure [45] of Janošević et al. [48] was applied for the synthesis of nanoPANI.DNSA precursor: 2.45 g of aniline was dissolved in 1140 ml of aqueous solution containing 3.01 g of DNSA and the solution was heated to boiling, cooled to room temperature, and then the aqueous solutions of monomer and oxidant APS (7.53 g, 60 ml) were mixed to start the oxidation, and the reaction mixture was stirred for 24 h. The precipitated nanoPANI-DNSA was collected on a filter, rinsed with 1.6×10^{-2} M DNSA and dried in vacuum. All syntheses of PANIs were performed at room temperature. The precursors nanoPANI, nanoPANI.SSA and nanoPANI.DNSA were then carbonized by means of gradual heating in a nitrogen atmosphere up to 800 °C at a heating rate of 10 °C min⁻¹ to obtain C-PANI, C-PANI.SSA and C-PANI.DNSA, respectively. A Carbolite CTF 12/75/700 tube furnace with temperature regulation by Eurotherm 815P Prog/Controller was used for the carbonization.

2.2. Characterization: morphology, elemental composition, structure and conductivity

A scanning electron microscope (SEM) JEOL JSM 6610 LV was used to characterize the morphology of the samples. Powdered materials were deposited on adhesive tape fixed to specimen tabs and then ion-sputter-coated with gold using a BAL-TEC SCD 005 Sputter Coater prior to SEM measurements.

Elemental analysis (C, H, N, and S) was carried out by the Elemental Analyzer Vario EL III (Elementar). The content of oxygen was determined by difference.

XPS spectra were recorded on a Kratos Axis Ultra DLD (Kratos Analytical, Manchester U.K.), using monochromatic Al K α X-rays (1486.69 eV) with X-ray power of 150 W. Survey spectra were collected with 160 eV pass energy, whilst core-level scans were collected with pass energy of 20 eV. The base pressure in the system was 2×10^{-9} Torr. The analysis area for the data collection using the hybrid electrostatic and magnetic lens system and the slot aperture is approximately 300 × 700 mm. Data analysis was performed using CasaXPS using Kratos' relative sensitivity factors. Core-level scans were calibrated based on a peak fit to the C1s scan, with the component due to aromatic carbon set to 284.7 eV. Shirley backgrounds were used throughout. Gaussian–Lorentzian product lineshapes were used with 30% Lorentzian weighting.

Raman spectra were collected on a Thermo Scientific DXR Raman microscope, equipped with an Olympus optical microscope and a CCD detector. A diode-pumped solid-state laser with excitation wavelength of 532 nm was used. Raman spectra were fitted within 900 and 1840 cm⁻¹ using two Gaussian components for G

and D band. The results of the fit were numerically integrated to obtain the area of both G and D bands.

The X-ray powder diffraction measurements were performed on a Philips 1050 X-ray powder diffractometer using Ni-filtered Cu K α radiation and Bragg–Brentano focusing geometry. The patterns were collected in 2θ range from 5° to 65° with the step of 0.05° and exposure time of 10 s per step.

The electrical conductivity was measured at room temperature by means of an ac bridge Wayne Kerr Universal Bridge B 224, operating at fixed frequency of 1.0 kHz. During the measurement powders were compressed between stainless pistons, within an insulating hard-plastic tube, at the constant pressure of 124 MPa.

2.3. Determination of textural parameters: N_2 sorption

Nitrogen adsorption–desorption isotherms obtained at 77 K were used to estimate textural properties of carbonized PANI samples. Micropore volume (pores with diameter < 2 nm, V_{mic}) was estimated using the Dubinin–Raduskevich method [49], while micropore surface (S_{mic}) was obtained using Kaganer's modification of Dubinin's theory [49]. Mesopore ($2 \text{ nm} < \text{diameter} < 50 \text{ nm}$) volumes (V_{meso}) and mesopore surfaces (S_{meso}) were estimated according to the Dollimore and Heal method as described in [46]. Estimate of real specific surface areas (S_{tot}) of studied samples were then obtained as the sum of S_{mic} and S_{meso} . Since all three studied carbonized PANIs are dominantly microporous materials [46], and the BET method is not best suited to estimate the specific surface area of such materials [49], the values of S_{tot} obtained in this way are considered to be more reliable than the specific surface area values obtained using BET method (S_{BET}). The values of S_{BET} are also enclosed for comparison.

2.4. Electrochemical measurements

The surface of a glassy carbon (GC) rotating disc (0.196 cm^2) was used to support the catalyst. The GC disc was polished to a mirror finish with an alumina suspension before each experiment. The catalyst ink was prepared by dispersing desirable amount of PANI-derived N-doped carbon nanomaterials in ethanol/water mixture (40 v/v%). After homogenization in an ultrasonic bath for 30 min, 10 μl of the catalyst ink was transferred onto the GC surface, covered with 10 μl of 0.05 wt% Nafion, and dried. Depending on the amount of dispersed nanocarbon, anticipated catalyst loadings were 250 and 500 $\mu\text{g cm}^{-2}$. The solvent was then removed by evaporation in an argon stream. For electrochemical investigations, a conventional, three-electrode cell was used. A wide Pt foil served as a counter electrode and a saturated calomel electrode (SCE) served as a reference electrode. A Gamry PCI4/750 Potentiostat/Galvanostat equipped with a Pine rotator was used for voltammetric investigations. The electrolyte solutions, 0.1 mol dm^{-3} KOH, were saturated by either nitrogen or oxygen gas of high purity (99.999 vol.%). During the measurements, a gentle gas flow was introduced just beneath the electrolyte surface. The ORR was investigated using a rotating disk electrode (RDE), at the rotation rates between 300 and 3600 rpm. The potential was swept within the limits +0.27 to −0.97 V vs. SCE at 20 mV s^{-1} , unless specified otherwise. Current densities are evaluated with respect to geometrical cross section area of supporting GC disk.

3. Results and discussion

3.1. Morphology and electrical conductivity of the samples

The SEM pictures of all PANI salt precursors before and after carbonization indicate that the carbonization caused almost

negligible changes in morphology [10,42,45]. The morphology of carbonized PANI samples obtained from various precursors (Fig. 1) shows a substantial degree of similarity, with nanocylinders (nanorods/nanotubes) as a dominant particle form [10,42,45]. However, certain differences in their morphologies should be pointed out. Namely, C-PANI.SSA shows the most homogenous morphology with elongated nanocylinders and only a few shorter and agglomerated nanocylinders (Fig. 1A), C-PANI shows only shorter agglomerated nanocylinders, frequently deposited on nanosheets (Fig. 1B), while C-PANI.DNSA has a form of shorter and elongated nanorods (Fig. 1C) [45,46]. The diameter of nanorods decreases in the order $d_{\text{C-PANI.SSA}}$ (85–220 nm) $\geq d_{\text{C-PANI.DNSA}}$

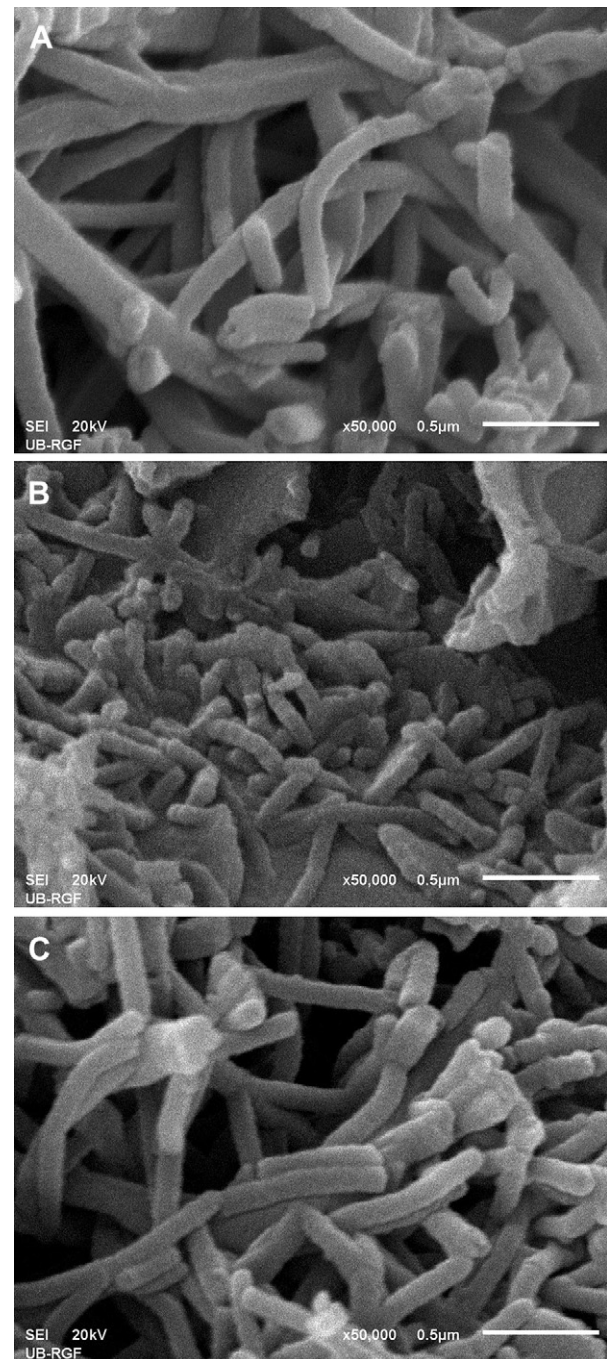


Fig. 1. SEM images of (A) C-PANI.SSA, (B) C-PANI and (C) C-PANI.DNSA (white bar length 0.5 μm ; magnification $\times 50,000$).

(50–150 nm) > $d_{\text{C-PANI}}$ (35–75 nm). Our previously published TEM measurements [46] revealed that C-PANI.SSA and C-PANI contain a fraction of nanotubes (hollow nanocylinders) besides prevalent nanorods, while C-PANI.DNSA contains only nanorods. Nanotubes have an outer diameter 95–250 nm for C-nanoPANI-SSA and ~100 nm for C-nanoPANI, while the diameter of their inner hollow channels amounts to 10–50 nm for C-nanoPANI-SSA and ~40 nm for C-nanoPANI. Granular fraction is also present in all samples.

In addition to the differences in morphology, electrical conductivities of investigated carbon nanomaterials also differ: C-PANI.SSA has significantly higher conductivity (0.85 S cm^{-1}) compared to other two samples (0.35 and 0.32 S cm^{-1} for C-PANI.DNSA and C-PANI, respectively) [46].

3.2. XRD analysis

XRD patterns of investigated samples (Fig. 2) indicate quite similar phase composition. Two broad maxima evidenced in all diffractograms, centered around 2θ values of 24° and 44° , are attributed to the reflections of graphitic planes (002) and (101), respectively [50]. The most important common feature of XRD patterns is the presence of broad maximum at 24° which signifies the domination of disordered carbon phase in all studied carbonized nanostructured PANI samples, while the weak wide maximum at 44° suggests the existence of graphitic layers which have small sizes and low three-dimensional order [51]. Only the XRD pattern of C-PANI.DNSA exhibits weak narrow peaks at ~ 44° and ~ 50° which can be explained by the presence of a low amount of crystalline graphitic phase.

3.3. Raman spectra

Raman spectroscopy revealed that the molecular structures of all carbonized nanostructured PANI salts, similarly to their crystalline/amorphous phase compositions, are only slightly different. The Raman spectra of the investigated samples (Fig. 3) display characteristic features of carbonaceous materials [52], with two broad maxima centered around 1350 cm^{-1} and 1590 cm^{-1} . The peak at a lower wavenumber, usually referred to as the disorder-induced D-band, is due to the breathing vibrations of sp^2 sites in sixfold aromatic rings and it is commonly associated with structural defects and reduction in symmetry due to the incorporation of hetero-atoms inside the graphitic lattice. The second band at higher energy, the graphitic G-band, is attributed to the stretching

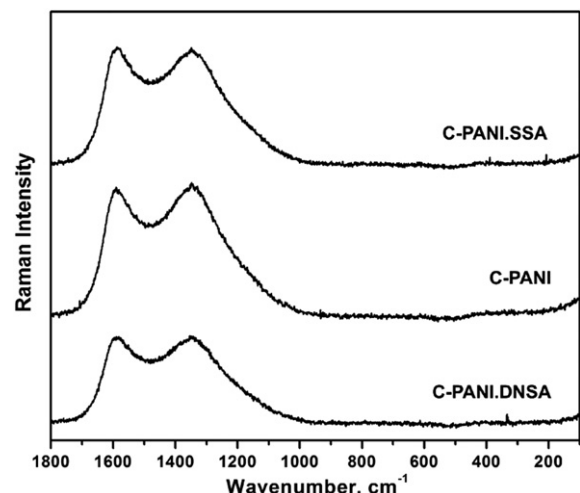


Fig. 3. Raman spectra of C-PANI.SSA, C-PANI and C-PANI.DNSA.

vibration of any pair of sp^2 sites inside the graphitic pattern. The ratio between D and G bands intensities (I_D/I_G) can be used to assess the degree of structural defects present in carbonaceous material. The I_D/I_G ratios for C-PANI, C-PANI.DNSA and C-PANI.SSA, determined using integrated peak areas, are found to be 3.48, 3.68 and 3.56, respectively. These Raman spectral data indicate both the low increase of graphitic lattice defects in the order C-PANI < C-PANI.SSA < C-PANI.DNSA and the significant disorder in all samples due to the extensive nitrogen and oxygen incorporation in the carbon sp^2 network, known to be beneficial for ORR [53,54].

3.4. XPS analysis

The significance of surface N-containing functional groups for efficient ORR electrocatalysis by N-doped carbon materials has been demonstrated by many research groups [54–57]. However, the unambiguous answer to the question about the role and significance of various surface nitrogen functional groups in ORR catalysis is still missing [12–21]. Therefore, C-PANI, C-PANI.SSA, and C-PANI.DNSA with empirical formulas $\text{C}_{30}\text{H}_{10}\text{N}_3\text{O}_4$, $\text{C}_{67}\text{H}_{18}\text{N}_7\text{O}_5$, and $\text{C}_{64}\text{H}_{21}\text{N}_7\text{O}_7$, respectively, as determined by elemental analysis (Table 1) [10,44,45], were examined by XPS (see Supporting Information, Fig. S1 for complete XPS spectra) in order to determine surface functional groups and the surface atomic concentration (Table 1). Both the surface nitrogen and carbon contents increase in the order C-PANI.DNSA < C-PANI < C-PANI.SSA, while the surface oxygen content decreases in the same order (Table 1).

Taking into account the fact that XPS determines the surface elemental composition while elemental analysis determines the bulk elemental composition, results of elemental analysis [10,44,45] and XPS (Table 1) indicate heterogeneous molecular structures of prepared carbonized PANI samples, which generally have significantly higher surface carbon content (at.%) than the bulk carbon content (at.%) due to the much more efficient carbonization of the shell of PANI nanostructures than of their interior parts.

Several surface carbon and nitrogen groups are identified by deconvolution of their respective C1s and N1s XPS signals (Fig. 4). Asymmetry in the C1s peak and its shift to higher binding energies [38,53], compared to sp^2 hybridized graphitic carbon, corresponds to the already confirmed nitrogen incorporation. To achieve adequate deconvolution, the C1s peak was broken down into five components. The first peak, located at 284.7 eV, is usually attributed to sp^2 hybridized carbon [53]. The peaks centered around 285.8 eV and 287.0 eV are interpreted as the sp^2 and sp^3 hybridized carbon

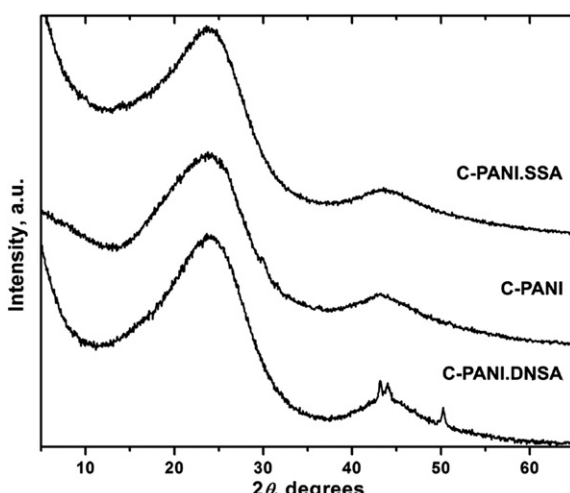


Fig. 2. XRD patterns of C-PANI.SSA, C-PANI and C-PANI.DNSA.

Table 1

The elemental composition of C-PANI.SSA, C-PANI and C-PANI.DNSA, determined by the XPS analysis and the elemental microanalysis.

C-PANI.SSA		C-PANI		C-PANI.DNSA	
XPS [46], at.%	Elemental analysis, at.%	XPS [46], at.%	Elemental analysis, at.%	XPS [46], at.%	Elemental analysis, at.%
Carbon	88.3	84.7	87.9	80.4	87.6
Nitrogen	7.0	9.0	5.8	8.2	5.5
Oxygen	4.6	6.3	6.3	11.4	7.0

bonded to sp^2 and sp^3 hybridized nitrogen, respectively [56]. The peak centered at 288.4 eV is attributed to carbon of carboxyl or ester groups, while the peak at 289.9 eV corresponds to carbon of carbonate groups and/or adsorbed CO and CO_2 [58]. Binding energies around 398.3 eV, 400.7 eV, and between 402.6 and 404.4 eV of the peaks obtained by the deconvolution of N1s signal, are identified as pyridinic nitrogen (N-6), quaternary nitrogen (N-Q), and N-oxide nitrogen ($\text{N}^+ - \text{O}^-$), respectively [46]. Additionally, the peaks at 396.5 eV and 399.7 eV are assigned to tetrahedral sp^3 nitrogen bonded to sp^3 carbon (N-1) [59] and pyrrolic nitrogen (N-5) [60,61], respectively. Based on the contribution of individual nitrogen and carbon group type to the overall surface concentration, calculated on the basis of the area of their respective peaks, it can be concluded that pyridinic and quaternary nitrogen atoms are the dominant surface nitrogen species, while $\text{C}=\text{N}$ and graphitic $\text{C}=\text{C}/\text{C}-\text{C}$ are prevalent carbon species at the surface of all carbonized PANI salts. The ratio of $\text{C}=\text{N}$ to graphitic $\text{C}=\text{C}/\text{C}-\text{C}$ surface carbon content is almost the same for all investigated carbonized PANI salts (19.8–22.6% C atoms in $\text{C}=\text{N}$ vs. 64.0–66.4% C atoms in $\text{C}=\text{C}/\text{C}-\text{C}$). It is important to note that the surface content of pyridinic nitrogen is higher than the surface content of quaternary nitrogen in the case of C-PANI.SSA (51.3 vs. 39.0% N atoms), while this ratio has the opposite trend in the case of C-PANI (35.0 vs. 40.9% N atoms) and C-PANI.DNSA (40.9 vs. 50.6% N atoms).

3.5. Textural parameters

All three studied materials have practically the same specific pore volume regarding the pores up to 50 nm in diameter, as can be

seen by adding V_{mic} to V_{meso} (amounting to roughly $0.205 \text{ cm}^3 \text{ g}^{-1}$, Table 2). However, individual contribution of micropores $V_{\text{mic}}/(V_{\text{mic}} + V_{\text{meso}})$ decreases from C-PANI.DNSA (90%) to C-PANI (66%) and C-PANI.SSA (63%) [46]. Both the specific surface area (estimated either as S_{tot} or S_{BET}), and the micropore surface area, S_{mic} , decrease also in the order C-PANI.DNSA > C-PANI > C-PANI.SSA. It is important to note that all three materials are essentially microporous, but C-PANI and C-PANI.SSA contain also a significant contribution of mesopores [46]. The order of increase of V_{meso} and S_{meso} is opposite to the order of increase of V_{mic} and S_{mic} , i.e. the highest content of mesopores is observed for C-PANI.SSA.

The results acquired so far unambiguously reflect the influence of different molecular and supramolecular structure of PANI precursors containing different counter-ions on the morphology, surface elemental composition, surface functional groups, pore structure and electrical conductivity of PANI-derived carbon nanomaterials.

3.6. Electrochemical characterization – ORR performance

Structural, morphological and textural differences of investigated N-containing carbon nanomaterials, caused by the differences in molecular structure and properties of corresponding PANI salt precursors, are reflected in their different capacitive properties, as observed from blank cyclic voltammograms of PANI-derived-nanocarbons-modified GC electrodes in a nitrogen purged 0.1 mol dm^{-3} KOH solution (Fig. 5). The differences in pseudocapacitance observed within the potential limits -0.25 to -1 V vs. SCE, especially in the potential windows between -0.5 and -0.25 V

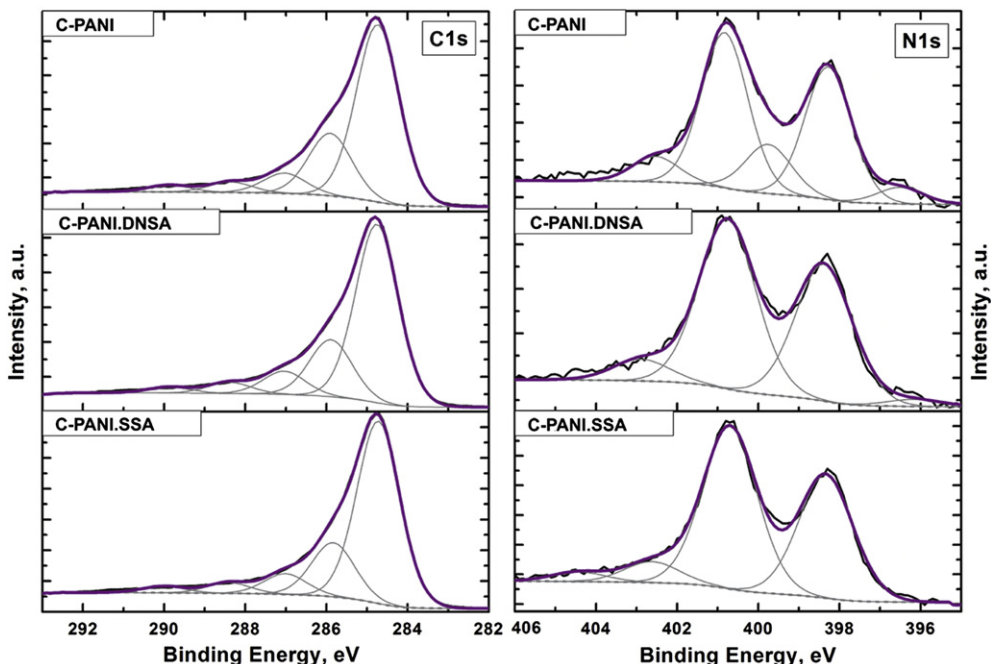


Fig. 4. Fitted high-resolution XPS C1s and N1s spectra of C-PANI, C-PANI.DNSA and C-PANI.SSA.

Table 2
Textural properties of studied materials.

	C-PANI.SSA	C-PANI	C-PANI.DNSA
$V_{\text{mic}} (\text{cm}^3 \text{g}^{-1})$	0.128	0.138	0.185
$S_{\text{mic}} (\text{m}^2 \text{g}^{-1})$	360	388	520
$V_{\text{meso}} (\text{cm}^3 \text{g}^{-1})$	0.076	0.071	0.020
$S_{\text{meso}} (\text{m}^2 \text{g}^{-1})$	50	48	21
$S_{\text{BET}} (\text{m}^2 \text{g}^{-1})$	317	322	441
$S_{\text{tot}} (\text{m}^2 \text{g}^{-1})$	410	436	541
$V_{\text{mic}}/(V_{\text{mic}} + V_{\text{meso}}) (\%)$	62.7	66.0	90.2

vs. SCE, as well as between -1 and -0.75 V vs. SCE, can be ascribed to a mutual interplay of different nitrogen functionalities incorporated into the material surface and different pore sizes in these three carbon nanomaterials, resulting in dissimilar accessibility of nitrogen sites under electrochemical conditions [46].

Corresponding ORR RDE polarization curves in O_2 -saturated 0.1 mol dm^{-3} KOH for the catalyst loading of $250 \mu\text{g cm}^{-2}$ (Fig. 6), indicate large differences in ORR activity of the three investigated PANI-derived carbon nanomaterials. This statement holds regardless on the rotation rate. The ORR activity was found to increase from C-PANI.DNSA via C-PANI to C-PANI.SSA. The onset potential for O_2 reduction for C-PANI.DNSA is about -0.22 V vs. SCE and the reduction current gradually increases with more negative potentials. RDE curves for C-PANI and C-PANI.SSA both show noticeably improved behavior compared to C-PANI.DNSA. Enhanced reduction kinetics is evident in the more positive onset potentials, amounting to -0.18 V and -0.15 V vs. SCE for C-PANI and C-PANI.SSA, respectively. This is a first indication that both C-PANI and C-PANI.SSA present excellent electrocatalytic materials for ORR in alkaline media. Also, higher current densities for ORR at a given rotation

rate, observed for the last two materials, imply improved kinetics pointing to a higher number of electrons involved in O_2 reduction.

The RDE data were processed using Koutecky–Levich (K–L) analysis [62]. It presents an elegant alternative to the rotating ring-disk technique, allowing the determination of number of electrons consumed per O_2 molecule (n), giving an insight into the mechanism of ORR. Number of electrons is determined from the slope of K–L lines defined by:

$$\frac{1}{j} = \frac{1}{j_k} + \frac{1}{j_d} = \frac{1}{j_k} - \frac{1}{0.62 \cdot n \cdot F \cdot D^{2/3} \cdot \nu^{-1/6} \cdot \omega^{1/2} \cdot c} \quad (1)$$

In Eq. (1) j , j_k and j_d are the measured current density, kinetic current density and the limiting diffusion current density. Furthermore, ν presents the kinematic viscosity and D is the diffusion coefficient of diffusing species whose concentration is given by c . Usual literature values of these parameters [63] were used for the K–L analysis based on Eq. (1). The K–L plots of O_2 reduction, measured on each of the three samples (Fig. 6, inset top right), display linear course and the ordinate intercepts different than zero, suggesting that, for all three materials, in the entire potential window, the O_2 reduction process is under mixed kinetic-diffusion control. The K–L analysis revealed markedly different catalytic properties of the three investigated carbon nanomaterials. For C-PANI.DNSA K–L analysis showed that ORR proceeds through a $2e^-$ pathway (Fig. 6, inset bottom right). Based on this result, this material can be considered as a very good candidate for the electrochemical synthesis of hydrogen peroxide in alkaline solution [45]. If we look at the other two samples, the value of n is higher than 2 (Fig. 6, inset bottom right), which suggests that the peroxide formed is, at least partly, reduced further to $\text{H}_2\text{O} (\text{OH}^-)$. The number of electrons, n , increases with the decrease of the electrode potential for both C-PANI.SSA and C-PANI. If we compare C-PANI.SSA to C-PANI, higher n was found at all potentials for C-PANI.SSA, as expected from RDE results (Fig. 6). This makes C-PANI.SSA and C-PANI excellent ORR electrocatalysts with comparable properties to recently reported vertically aligned N-containing carbon nanotubes (NCNTs) [36] with the ORR onset potential around -0.15 V vs. SCE in 0.1 M KOH and n around 3 at potentials above -0.8 V vs. SCE. The NCNTs prepared in various ways were reported to display ORR onset potential of -0.1 V vs. Ag/AgCl (-0.145 vs. SCE) electrode in alkaline solution with an n value between 2.76 and 3.63, depending on the preparation mode (n was calculated for $E = -0.5$ V vs. Ag/AgCl, i.e. -0.545 V vs. SCE) [64]. The results obtained here are also comparable with the ones for NCNTs synthesized using different aliphatic diamines as nitrogen–carbon precursor solutions [34]. Onset potentials of C-PANI.SSA and C-PANI are similar or better than the ones of NCNTs synthesized by a single step chemical vapor deposition technique using either ferrocene or iron(II) phthalocyanine as catalyst and pyridine as the carbon and nitrogen precursor [39]. In comparison to different nanostructured carbon materials studied by Kruusenberg et al. [64] both C-PANI.SSA and C-PANI display onset potentials up to even 100 mV more positive, with increased number of electrons consumed per O_2 molecule in the investigated potential window. These comparisons demonstrate applicability of the investigated carbon materials in low-temperature fuel cells and metal-air batteries.

The methodology applied here for the evaluation of catalyst activity toward ORR activity must be considered with the effects of catalyst loading. Subramanian et al. [65] emphasized the importance of this effect in the case of carbon-based nanocatalysts, and this effect was observed in the present study in the case of PANI-derived carbon nanomaterials, too. Upon doubling catalyst loading to $500 \mu\text{g cm}^{-2}$ (see Supporting Information, Fig. S2), in RDE voltammograms of ORR, compared to the case of loading of

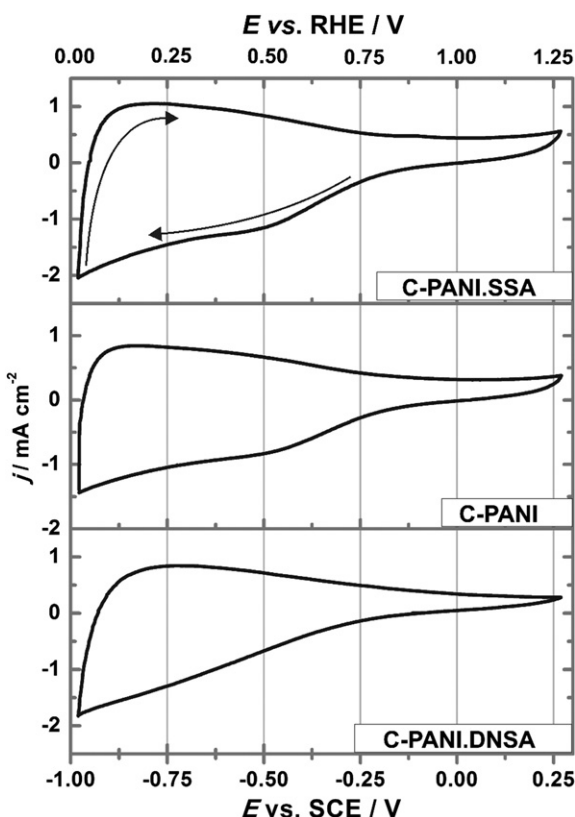


Fig. 5. Cyclic voltammograms of PANI-derived-nanocarbon-modified GC electrodes in N_2 purged 0.1 mol dm^{-3} KOH (loading $500 \mu\text{g cm}^{-2}$, sweep rate 20 mV s^{-1}).

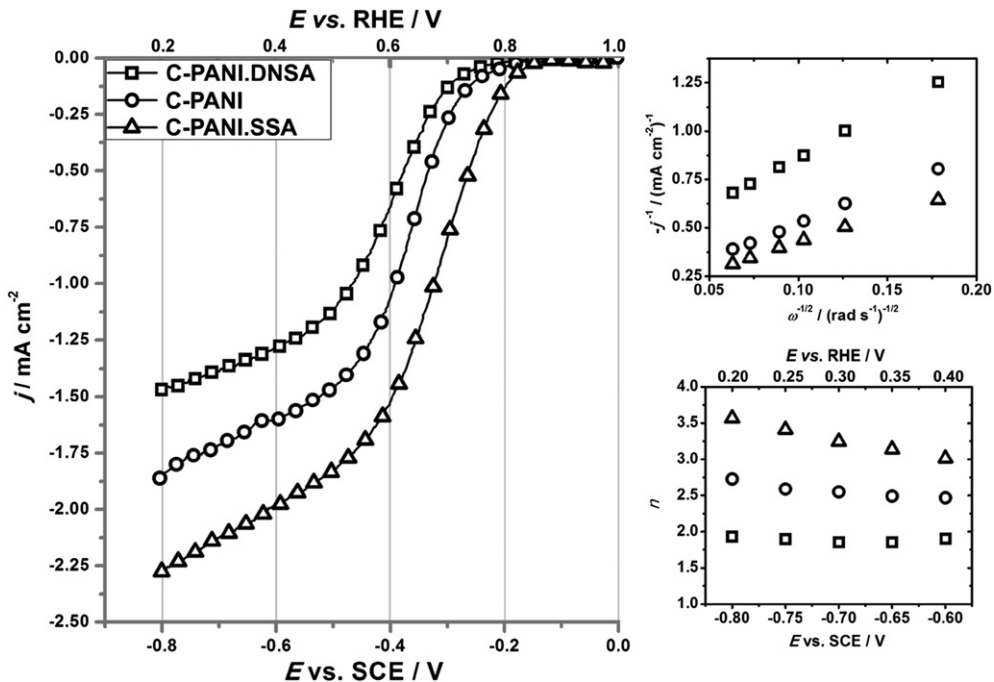


Fig. 6. Background-corrected RDE voltammograms of oxygen reduction (sweep in anodic direction) on PANI-derived-nanocarbon-modified GC electrodes in O_2 -saturated 0.1 mol dm^{-3} KOH (loading $250 \mu\text{g cm}^{-2}$; rotation rate 600 rpm , sweep rate 20 mV s^{-1}). Insets are the Koutecky–Levich plots at -0.6 V vs. SCE (top right) and the estimated number of electrons (bottom right).

$250 \mu\text{g cm}^{-2}$, three distinct effects may be observed for all three studied materials (Fig. 6): (i) ORR onset potential shifts toward more positive potentials, (ii) higher ORR currents are being measured and (iii) the number of electrons consumed per O_2 molecule increases, as found by K–L analysis. All these effects reveal a significant improvement of electrocatalytic activity with increase of catalyst loading (see Supporting Information, Fig. S3 for detailed discussion). ORR onset potentials measured for the catalyst loading of $500 \mu\text{g cm}^{-2}$ amounted to -0.05 , -0.12 and -0.1 V vs. SCE for C-PANI.SSA, C-PANI and C-PANI.DNSA, respectively. The highest onset potential was evidenced in the case of C-PANI.SSA, pointing to its high intrinsic activity toward ORR. The increase of catalyst loading yielded to increased ORR RDE currents and number of electrons consumed per O_2 molecule, in accordance with the previous reports [66].

3.7. Relationship between electrocatalytic performance and material properties and new insights into the mechanism of ORR on N-doped carbon nanomaterials

The overall improvement of ORR performance can be correlated to the increase of both the total surface nitrogen concentration and the content of pyridinic nitrogen functional groups (Table 1, Section 3.4). The improvement effect is most prominent for C-PANI.SSA, with 7.04 at.% surface nitrogen atoms (3.61 at.% being in the pyridinic form), which displays the most positive onset potential. More negative onset potentials of C-PANI and C-PANI.DNSA can be attributed to lower surface nitrogen content, 5.83 at.% (2.04 at.% in pyridinic form) and 5.5 at.% (2.25 at.% in pyridinic form), respectively. Interestingly, C-PANI has a more positive onset potential despite having lower pyridinic nitrogen fraction than C-PANI.DNSA, 2.04 at.% vs. 2.25 at.%. Similar discrepancies have previously been ascribed: i) to the possible changes of the bulk properties of NCNTs induced by nitrogen incorporation and consequent increase in electronic conductivities [67,68], ii) to the possible contribution of active N–C functionalities other than pyridinic [69] and iii) to the

enhanced reactant and intermediate adsorption [37,70]. Although differences in electronic conductivities can stand in favor of high ORR activity of C-PANI.SSA, practically the same conductivities were found for C-PANI and C-PANI.DNSA. On the other hand, significant differences are found in the pore structure of studied materials. Hence, besides desirable nitrogen surface functionalities, total surface nitrogen and electrical conductivity, availability of the active sites must be assured by appropriate pore structure. The results suggest that a high degree of microporosity of C-PANI.DNSA [45,46] hinders the electrochemical response of this material in terms of ORR activity by reducing the access of molecular O_2 to the active sites within micropores. We suspect that the ORR proceeds mainly on the surface of carbon particles and in mesopores, while reacting species/products of ORR very slowly reach the active sites inside micropores. A similar conclusion was made by Kruusenberg et al. in their study of ORR in alkaline media (0.1 M KOH) on GC electrode modified with multiwalled carbon nanotubes, carbon black powder, and two carbide-derived carbons [64]. Looking at the high current density region (Fig. 6), it is clear that higher surface nitrogen content leads to an increase of current densities at deep negative potentials. The increased nitrogen content was correlated earlier to higher limiting ORR current densities with only minor effect on the ORR in the kinetic regime, without providing textural characteristics of studied materials [71]. Nevertheless, in the light of the importance of pore structure it is fairly difficult to fully resolve all the relevant factors governing ORR kinetics. The possibility that pore size can reimburse for incorporation of nitrogen in exterior surface layers cannot be rejected. In order to demonstrate the importance of both nitrogen incorporation and proper textural characteristics we have evaluated mass activities (I_{mass}) at the high current density region of studied materials and correlated them with certain structural and textural materials' properties (Fig. 7).

As one may see (Fig. 7A), there is an almost linear correlation between I_{mass} with S_{meso} , while the total surface nitrogen content can only provide a good overall trend (Fig. 7B). As already mentioned, there is a certain discrepancy between the content of

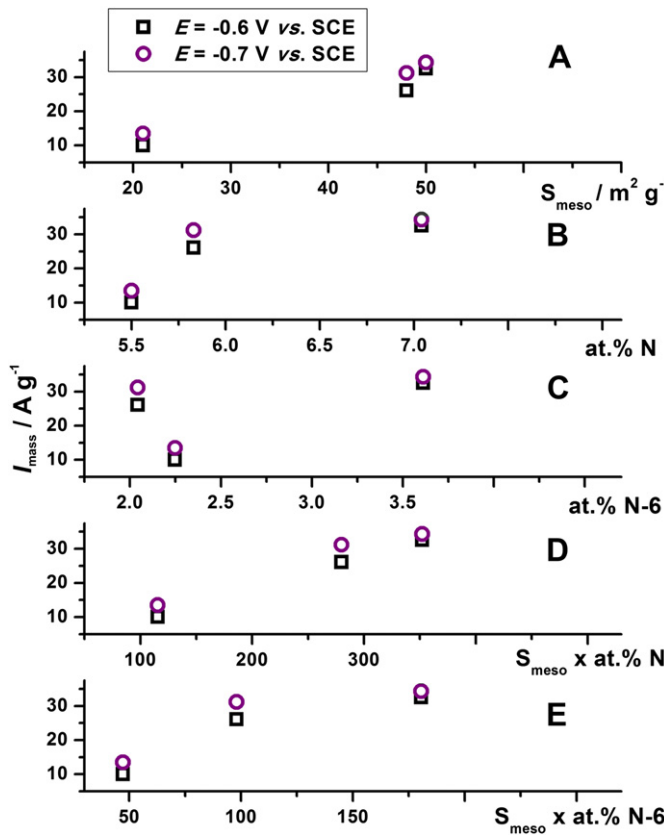


Fig. 7. Correlation of mass activities (I_{mass} , A g^{-1}) derived from K-L analysis with structural and textural characteristics of studied N-doped PANI-derived carbon nanomaterials.

surface pyridinic nitrogen (N-6) functionalities (Fig. 7C), considered to be of crucial importance, and ORR performance. However, when one considers both the mesopore surface area and the total nitrogen content (or N-6 surface content) very good correlations with I_{mass} are obtained (Fig. 7D, E). This supports the conclusion derived earlier: in order to achieve high ORR activity, active sites formed by nitrogen incorporation must be available to O_2 which can be made possible by appropriate pore structure. The actual mechanism of ORR acceleration by N-dopant is still open to discussion, especially due to the interplay between textural properties and nitrogen surface functionalities, being rather hard for separate investigation. However, two roles of action of N-dopant are anticipated: i) enhanced charge transfer kinetics and ii) altered energetics of interaction of reactive species and intermediates for ORR.

The effect of catalyst loading, demonstrated here and in the previously published paper [62], favors an interesting view regarding the actual mechanism of ORR on non-noble metal catalysts. Namely, an increase in the apparent number of electrons consumed per O_2 molecule can be considered as a consequence of the catalyst layer thickness which, if enlarged, may enhance the probability of peroxide transformation to water [66]. Nevertheless, here we deal with materials of similar density but rather different morphology, pore structure and with various relative contents of nitrogen surface functional groups. In agreement with the earlier works [37,72], it can reasonably be assumed that O_2 is being effectively reduced through a “pseudo” 4-electron pathway. If such a mechanism is effective, O_2 is electrochemically reduced to HO_2^- on the surface N-functionalities (most likely pyridinic, as commonly proposed [38,65]), followed by a catalytic regenerative process in which HO_2^- intermediate is chemically disproportionated to the

species OH^- and O_2 . We suggest that if the material is highly microporous, O_2 may be reduced to HO_2^- on the surface of carbon nanoparticles but not in the micropores and, under the conditions of increased mass transport rate operating in an RDE experiments, HO_2^- is quickly removed from the electrode surface, resulting in apparent 2-electron reduction. If the material has appreciable contribution of mesopores, HO_2^- is being formed in the mesopores too, and increased mass transfer rate has a lesser effect on the removal of intermediately formed HO_2^- , allowing more time for the chemical step of HO_2^- disproportionation to OH^- and O_2 to take place within the pores. Furthermore, chemically formed O_2 can further undergo the electrochemical reduction, leading to an increase in the apparent number of electrons above 2. In the case of metal-doped NCNTs, HO_2^- disproportionation was confirmed to be catalyzed by metal particles [72]. However, we believe that surface functional groups in metal-free N-containing carbon nanomaterials can also provide similar action improving ORR kinetics and raise the apparent number of electrons consumed per O_2 molecule above 2. An enlarged catalyst loading can act in the same way as a suitable pore size: a densely loaded catalyst can trap O_2 formed upon disproportionation step within interparticle voids (even in the case of microporous material) and provide improved ORR kinetics with a higher number of electrons consumed per O_2 molecule. To summarize, different apparent number of electrons consumed per O_2 and improved ORR kinetics by use of either specific carbon materials or specific carbon layers thickness does not necessarily mean the change in the mechanism of ORR. Namely, the changes in number of electrons might be invoked by textural properties of carbonaceous material and the catalyst layer thickness. This becomes rather important when catalytic activity trends have to be established for different materials. Theoretical calculations and detailed *in situ* research of surface reactions is needed to completely reveal the mechanism of oxygen reduction on nitrogen-rich carbons and the mechanism of ORR acceleration in the presence of N-dopant.

3.8. Relationship between material's capacitance and ORR performance

The factors governing the ORR activity of a particular material present the topic of active scientific debate. For example, the activity of Pt-based electrocatalysts for ORR has been considered to be determined by the onset of the surface oxidation process which stops ORR on these materials [73]. Here we have explained large differences in ORR activity of three studied N-containing nano-carbon materials by their textural differences and the presence of different surface nitrogen functional groups. Nevertheless, these three materials, besides excellent ORR activity, have the exceptional capacitive properties with gravimetric capacitances ranging from $\sim 120 \text{ F g}^{-1}$ (C-PANI.DNSA) to $\sim 400 \text{ F g}^{-1}$ (C-PANI.SSA) in 6 M KOH [46]. We believe that the build-up of the electrical double layer (EDL) in ORR experiments during potentiodynamic cycling cannot be considered separately from the ORR taking place on the electrode material.

In order to establish these effects in a qualitative manner we have analyzed blank cyclic voltammograms of C-PANI.SSA and C-PANI.DNSA recorded at different sweep rates (10, 50 and 100 mV s^{-1}) and normalized by a matching sweep rate (I/v) and corresponding background-corrected ORR RDE currents recorded at 10 and 50 mV s^{-1} (Fig. 8). This experiment was not intended to provide ORR kinetic parameters but to ascertain the effect of EDL build-up on ORR activity under different potentiodynamic conditions. The first noticeable difference observed when comparing normalized blank cyclic voltammograms of C-PANI.SSA and C-PANI.DNSA is much smaller difference between I/v curves upon

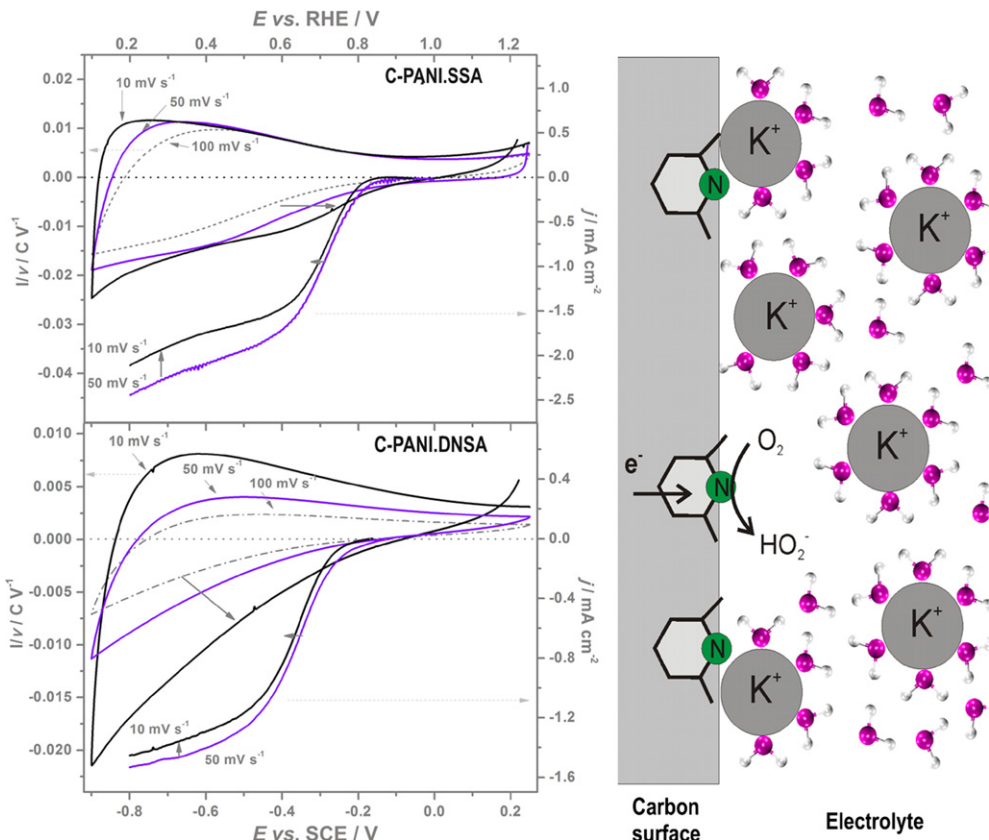


Fig. 8. Blank cyclic voltammograms of C-PANI.SSA (top) and C-PANI.DNSA (bottom) modified GC electrode in 0.1 M KOH recorded at different sweep rates (10, 50 and 100 mV s⁻¹) and normalized by a matching sweep rate (I/v) and corresponding background-corrected ORR RDE currents recorded at 10 and 50 mV s⁻¹ (rotation rate 600 rpm, catalyst loading 250 µg cm⁻²). On the right hand side a qualitative model describing blockage of ORR active sites is depicted. ORR can take place on non-blocked sites whose number is reduced if the electrode potential is swept slowly.

changing the sweep rate in the case of C-PANI.SSA (Fig. 8, top). As expected, increased capacitance is measured upon reducing sweep rate due to more time provided for ion diffusion inside meso- and micropores during EDL build-up [74]. In contrast, the capacitance of C-PANI.DNSA displays enormous increase upon reducing sweep rate from 100 mV s⁻¹ to 10 mV s⁻¹. Such a large difference is due to the difference in textural properties of the two materials, and the observed large increase of capacitance for C-PANI.DNSA is caused by the involvement of a large volume of micropores and slow EDL build-up. Simultaneously with the capacitance increase caused by the decrease in sweep rate, upon sweep rate was reduced from 50 mV s⁻¹ to 10 mV s⁻¹, we observed both the decrease of ORR onset potential and the drop in ORR currents in the high overvoltage region. This might seem contradictory to the earlier proposed “pseudo” 4-electron pathway. Namely one may reasonably expect, if electrode spends more time under polarization at which ORR takes place, large amounts of HO₂⁻ are disproportionated to O₂, which, entering the next charge transfer step, should enlarge n above 2. This controversy may be understood, i.e. resolved, in terms of EDL charging. Namely, during a slow potential sweep, more charge accumulates inside the EDL (Fig. 8), that blocks catalytically active sites and attenuates ORR, as actually observed. This agrees with the fact that, in the potential region of ORR emergence, the ORR onset potential shifts, and ORR current drops, simultaneously with the enlargement of the capacitive current (in Fig. 8, this behavior is illustrated by arrows). Interactions responsible for such behavior are pseudocapacitive interactions between the positively charged potassium cat ions and the nitrogen atoms in carbonaceous electrode material, considered to be highly liable

according to Hulicova et al. [75]. In addition, a more pronounced effect is observed in the case of C-PANI.SSA, although large changes of I/v curves in the case of C-PANI.DNSA might point the other way. This can be explained by the different textural characteristics of these two materials yet again. In the case of C-PANI.SSA, both EDL charging and ORR are enabled to take place on the nanoparticle surface and in mesopores, too. However, in the case of highly microporous C-PANI.DNSA, upon reduction of sweep rate, enlarged amount of the EDL charge accumulates within the hardly accessible micropores, causing I/v curves to increase, while ORR takes place predominantly on the outer nanoparticle surface. It is interesting to note that Strmcnik et al. [76] explained differences in ORR activity of Pt (111) electrode surface in different electrolytes (0.1 M LiOH, NaOH, KOH and CsOH) by the non-covalent interactions between hydrated alkali metal cations M⁺(H₂O)_x and adsorbed OH species which block active sites for ORR. We believe that similar effects are operative here, but they were invoked by changing the conditions of the potentiodynamic experiment, instead of changing the supporting electrolyte.

4. Conclusions

High diversity in the pore structure, total surface nitrogen content, and surface functional groups were evidenced for three studied carbonized PANI nanomaterials, denoted as C-PANI, C-PANI.DNSA, and C-PANI.SSA. These materials displayed quite different electrocatalytic properties toward ORR, with the apparent number of consumed electrons per O₂ molecule (n) between 2 and ~3.7. The large positive impact of the catalyst loading on the

electrocatalytic activity was evidenced, resulting in the shifting of the ORR onset potential, the number of electrons n , as well as the ORR currents toward higher values. At the catalyst loading amounting to $250 \mu\text{g cm}^{-2}$, among the three materials studied, C-PANI.SSA nanorods/nanotubes displayed both the highest onset potential, -0.15 V vs. SCE , and the highest number of electrons, 3–3.5, at potentials -0.6 and -0.8 V vs. SCE , respectively. At the catalyst loading amounting to $500 \mu\text{g cm}^{-2}$, the ORR onset potential for the same material increased to -0.05 V vs. SCE . The electrocatalytic activity of investigated carbonized PANI nanomaterials toward ORR in alkaline media was found to increase in the following order: C-PANI.DNSA < C-PANI < C-PANI.SSA. The observed electrochemical behavior of studied materials was explained in terms of “pseudo” 4-electron ORR pathway, in which O_2 is initially electrochemically reduced in a 2-electron process to form HO_2^- intermediate, which then undergoes further chemical disproportionation to form OH^- and O_2 . The presence of mesopores in the carbonized PANI nanomaterials allows ORR to take place inside the pores, where mass transfer is reduced and more time is available for chemically formed O_2 to undergo charge transfer. Within the frames of the actual mechanism of ORR on carbonaceous material, this leads to enlarged apparent number of electrons involved in ORR. The best ORR performance found for C-PANI.SSA is explained by the highest fraction of mesopores, the highest content of total surface nitrogen (7.04 at.%) and the highest surface content of pyridinic nitrogen functional groups. There are also strong indications that ORR performance estimated under potentiodynamic conditions is affected by the state of the electrical double layer of carbonized PANI electrodes.

We have demonstrated here that the application of different nanostructured PANI salts as precursors for synthesis of nitrogen-containing carbon nanomaterials can provide materials with quite different physico-chemical and electrocatalytic properties. This opens new perspectives in the fabrication of a series of N-containing carbon nanomaterials with exceptional electrode characteristics.

Acknowledgment

This work was supported by the Serbian Ministry of Education and Science (Contracts III45014 and OI172043). S.V.M. acknowledges the support provided by the Serbian Academy of Sciences and Arts through the project “Electrocatalysis in the contemporary processes of energy conversion”.

Appendix A. Supplementary material

Supplementary data related to this article can be found at <http://dx.doi.org/10.1016/j.jpowsour.2012.07.119>.

References

- [1] L. Zhang, J.J. Zhang, D.P. Wilkinson, H.J. Wang, *J. Power Sources* 156 (2006) 171–182.
- [2] A. Gewirth, M. Thorum, *Inorg. Chem.* 49 (2010) 3557–3566.
- [3] K. Gong, F. Du, Z. Xia, M. Durstock, L. Dai, *Science* 323 (2009) 760–764.
- [4] G. Wu, K.L. More, C.M. Johnstone, P. Zelenay, *Science* 332 (2011) 443–447.
- [5] J. Ozaki, S. Tanifuji, A. Furuichi, K. Yabutsuka, *Electrochim. Acta* 55 (2010) 1864–1871.
- [6] V. Nallathambi, J.W. Lee, S.P. Kumaraguru, G. Wu, B.N. Popov, *J. Power Sources* 183 (2008) 34–42.
- [7] G. Liu, X. Li, B.N. Popov, *ECS Trans.* 25 (2009) 1251–1259.
- [8] S.M. Lyth, Y. Nabae, S. Moriya, S. Kuroki, M. Kakimoto, J. Ozaki, S. Miyata, *J. Phys. Chem. C* 113 (2009) 20148–20151.
- [9] J.I. Ozaki, S.I. Tanifuji, N. Kimura, A. Furuichi, A. Oya, *Carbon* 44 (2006) 1324–1326.
- [10] A. Janošević, I. Pašti, N. Gavrilov, S. Mentus, G. Ćirić-Marjanović, J. Krstić, J. Stejskal, *Synth. Met.* 161 (2011) 2179–2184.
- [11] N. Gavrilov, M. Dašić-Tomić, I. Pašti, G. Ćirić-Marjanović, S. Mentus, *Mater. Lett.* 65 (2011) 962–965.
- [12] C.V. Rao, C.R. Cabrera, Y. Ishikawa, *J. Phys. Chem. Lett.* 1 (2010) 2622–2627.
- [13] L. Zhang, Z. Xia, *J. Phys. Chem. C* 115 (2011) 11170–11176.
- [14] S. Ni, Z. Li, J. Yang, *Nanoscale* 4 (2012) 1184–1189.
- [15] J. Vazquez-Arenas, D. Higgins, Z. Chen, M. Fowler, Z. Chen, *J. Power Sources* 205 (2012) 215–221.
- [16] H.S. Oh, J.G. Oh, W.H. Lee, H.J. Kim, H. Kim, *Int. J. Hydrogen Energy* 36 (2011) 8181–8186.
- [17] G. Liu, X. Li, P. Ganesan, B.N. Popov, *Electrochim. Acta* 55 (2010) 2853–2858.
- [18] D. von Deak, D. Singh, J.C. King, U.S. Ozkan, *Appl. Catal. B: Environ.* 113–114 (2012) 126–133.
- [19] H. Niwa, M. Kobayashi, K. Horiba, Y. Harada, M. Oshima, K. Terakura, T. Ikeda, Y. Koshigoe, J. Ozaki, S. Miyata, S. Ueda, Y. Yamashita, H. Yoshikawa, K. Kobayashi, *J. Power Sources* 196 (2011) 1006–1011.
- [20] H. Niwa, K. Horiba, Y. Harada, M. Oshima, T. Ikeda, K. Terakura, J. Ozaki, S. Miyata, *J. Power Sources* 187 (2009) 93–97.
- [21] S. Kundu, T.C. Nagaiah, W. Xia, Y. Wang, S. Van Dommele, J.H. Bitter, M. Santa, G. Grundmeier, M. Bron, W. Schuhmann, M. Muhler, *J. Phys. Chem. C* 113 (2009) 14302–14310.
- [22] S. Zhu, Z. Chen, B. Li, D. Higgins, H. Wang, H. Li, Z. Chen, *Electrochim. Acta* 56 (2011) 5080–5084.
- [23] Y. Li, J. Wang, X. Li, J. Liu, D. Geng, J. Yang, R. Li, X. Sun, *Electrochim. Commun.* 13 (2011) 668–672.
- [24] V. Neburchilov, H. Wang, J.J. Martin, W. Qu, *J. Power Sources* 195 (2010) 1271–1291.
- [25] J. Li, M.J. Vergne, E.D. Mowles, W.H. Zhong, D.M. Hercules, C.M. Lukehart, *Carbon* 43 (2005) 2883–2893.
- [26] E.N. Konyushenko, J. Stejskal, M. Trchová, J. Hradil, J. Kovářová, J. Prokeš, M. Cieslar, J.Y. Hwang, K.H. Chen, I. Sapurina, *Polymer* 47 (2006) 5715–5723.
- [27] T. Ramanathan, F.T. Fisher, R.S. Ruoff, L.C. Brinson, *Chem. Mater.* 17 (2005) 1290–1295.
- [28] J. Hu, P. Yang, C.M. Lieber, *Phys. Rev. B* 57 (1998) 3185–3188.
- [29] F. Le Normand, J. Hommet, T. Szörényi, C. Fuchs, E. Fogarassy, *Phys. Rev. B* 64 (2001) 2354161.
- [30] R. Droppa Jr., P. Hammer, A.C.M. Carvalho, M.C. dos Santos, F. Alvarez, *J. Non-Cryst. Solids* 299–302 (2002) 874–879.
- [31] S.E. Rodil, W.I. Milne, J. Robertson, L.M. Brown, *Appl. Phys. Lett.* 77 (2000) 1458–1460.
- [32] M. Bron, J. Radnik, M. Fieber-Erdmann, P. Bogdanoff, S. Fiechter, *J. Electroanal. Chem.* 535 (2002) 113–119.
- [33] C.H. Choi, S.H. Park, S.I. Woo, *Int. J. Hydrogen Energy* 35 (5) (2012) 4563–4570.
- [34] D. Higgins, Z. Chen, Z. Chen, *Electrochim. Acta* 56 (2011) 1570–1575.
- [35] G. Wu, M. Nelson, S. Ma, H. Meng, G. Cui, P.K. Shen, *Carbon* 49 (2011) 3972–3982.
- [36] N. Alexeyeva, E. Shulga, V. Kisand, I. Kink, K. Tammeveski, *J. Electroanal. Chem.* 648 (2010) 169–175.
- [37] S. Maldonado, K.J. Stevenson, *J. Phys. Chem. B* 109 (2005) 4707–4716.
- [38] P.H. Matter, L. Zhang, U.S. Ozkan, *J. Catal.* 239 (2006) 83–96.
- [39] Z. Chen, D. Higgins, Z. Chen, *Electrochim. Acta* 55 (2010) 4799–4804.
- [40] R.I. Jafri, N. Rajalakshmi, S. Ramaprabhu, *J. Power Sources* 195 (2010) 8080–8083.
- [41] G. Ćirić-Marjanović, in: A. Eftekhar (Ed.), *Nanostructured Conductive Polymers*, Wiley, London, 2010, pp. 19–98.
- [42] S. Mentus, G. Ćirić-Marjanović, M. Trchová, J. Stejskal, *Nanotechnology* 20 (2009) 245601.
- [43] M. Trchová, E.N. Konyushenko, J. Stejskal, J. Kovářová, G. Ćirić-Marjanović, *Polym. Degrad. Stab.* 94 (2009) 929–938.
- [44] N. Gavrilov, M. Vujković, I.A. Pašti, G. Ćirić-Marjanović, S.V. Mentus, *Electrochim. Acta* 56 (2011) 9197–9202.
- [45] A. Janošević, I. Pašti, N. Gavrilov, S. Mentus, J. Krstić, M. Mitrić, J. Travas-Sejdic, G. Ćirić-Marjanović, *Micropor. Mesopor. Mater.* 152 (2012) 50–57.
- [46] N. Gavrilov, I.A. Pašti, M. Vujković, J. Travas-Sejdic, G. Ćirić-Marjanović, S.V. Mentus, *Carbon* 50 (2012) 3915–3927.
- [47] A. Janošević, G. Ćirić-Marjanović, B. Marjanović, P. Holler, M. Trchová, J. Stejskal, *Nanotechnology* 19 (13) (2008) 135606 (8 pp.).
- [48] A. Janošević, G. Ćirić-Marjanović, B. Marjanović, M. Trchová, J. Stejskal, *Mater. Lett.* 64 (2010) 2337–2340.
- [49] S.J. Gregg, K.S.W. Sing, *Adsorption, Surface Area and Porosity*, vol. 41, Academic Press, London, 1982.
- [50] J. Yin, X. Xia, L. Xiang, X. Zhao, *Carbon* 48 (2010) 2958–2967.
- [51] M. Bystrzejewski, M.H. Rummeli, T. Gemming, H. Lange, A. Huczko, *New Carbon Mater.* 25 (2010) 1–8.
- [52] J. Robertson, *Mater. Sci. Eng. R* 37 (4–6) (2002) 129–281.
- [53] S. Maldonado, S. Morin, K.J. Stevenson, *Carbon* 44 (2006) 1429–1437.
- [54] S. Maldonado, K.J. Stevenson, *J. Phys. Chem. B* 108 (2004) 11375–11383.
- [55] P.H. Matter, E. Wang, M. Arias, E.J. Biddinger, U.S. Ozkan, *J. Phys. Chem. B* 110 (2006) 18374–18384.
- [56] K.Y. Chun, H.S. Lee, C.J. Lee, *Carbon* 47 (2009) 169–177.
- [57] Y.G. Lin, Y.K. Hsu, C.T. Wu, S.Y. Chen, K.H. Chen, L.C. Chen, *Diam. Relat. Mater.* 18 (2009) 433–437.
- [58] Z.R. Yue, W. Jiang, L. Wang, S.D. Gardner, C.U. Pittman Jr., *Carbon* 37 (1999) 1785–1796.

[59] H. Liu, Y. Zhang, R. Li, X. Sun, S. Désilets, H. Abou-Rachid, M. Jaidann, L.-S. Lussier, Carbon 48 (5) (2010) 1498–1507.

[60] I. Bertóti, I. Mohai, M. Mohai, J. Szépvölgyi, Diamond Relat. Mater. 20 (2011) 965–968.

[61] R. Pietrzak, Fuel 88 (2009) 1871–1877.

[62] A.J. Bard, L.R. Faulkner, Electrochemical Methods, second ed. Wiley, New York, 2001.

[63] V. Stamenkovic, T.J. Schmidt, P.N. Ross, N.M. Markovic, J. Electroanal. Chem. 554–555 (2003) 191–199.

[64] I. Kruusenberg, J. Leis, M. Arulepp, K. Tammeveski, J. Solid State Electrochem. 14 (2010) 1269–1277.

[65] N. Subramanian, X. Li, V. Nallathambi, S. Kumaraguru, H. Colon-Mercado, G. Wu, J. Lee, B. Popov, J. Power Sources 188 (2009) 38–44.

[66] A. Bonakdarpour, M. Lefevre, R. Yang, F. Jaouen, T. Dahn, J.-P. Dodelet, J.R. Dahn, Electrochim. Solid State Lett. 11 (2008) B105–B108.

[67] Y. Shao, J. Sui, G. Yin, Y. Gao, Appl. Catal. B: Environ. 79 (2008) 89–99.

[68] L.S. Panchakarla, A. Govindaraj, C.N.R. Rao, ACS Nano 1 (2007) 494–500.

[69] E. Biddinger, D. von Deak, U. Ozkan, Top. Catal. 52 (2009) 1566–1574.

[70] V.V. Strelko, N.T. Kartel, I.N. Dukhno, V.S. Kuts, R.B. Clarkson, B.M. Odintsov, Surf. Sci. 548 (2004) 281–290.

[71] Z. Chen, D. Higgins, Z. Chen, Carbon 48 (2010) 3057–3065.

[72] J.D. Wiggins-Camacho, K.J. Stevenson, J. Phys. Chem. C 115 (2011) 20002–20010.

[73] V.R. Stamenkovic, B. Fowler, B.S. Mun, G. Wang, P.N. Ross, C.A. Lucas, N.M. Marković, Science 315 (2007) 493–497.

[74] E. Raymundo-Piñero, K. Kierzek, J. Machnikowski, F. Béguin, Carbon 44 (2006) 2498–2507.

[75] D. Hulicova, M. Kodama, H. Hatori, Chem. Mater. 18 (2006) 2318–2326.

[76] D. Strmcnik, K. Kodama, D. van der Vliet, J. Greeley, V.R. Stamenkovic, N.M. Marković, Nat. Chem. 1 (2009) 466–472.